Human Molecular Genetics, 2016, Vol. 25, No. 18 3998–4011

doi: 10.1093/hmg/ddw240
Advance Access Publication Date: 27 July 2016
Original Article

ORIGINAL ARTICLE

An inactivating mutation in intestinal cell kinase, *ICK*, impairs hedgehog signalling and causes short rib-polydactyly syndrome

S. Paige Taylor[1,†], Michaela Kunova Bosakova[2,†], Miroslav Varecha[2], Lukas Balek[2], Tomas Barta[3], Lukas Trantirek[4], Iva Jelinkova[2], Ivan Duran[5,6,7], Iva Vesela[8], Kimberly N. Forlenza[5,6,7], Jorge H. Martin[5,6,7], Ales Hampl[3], University of Washington Center for Mendelian Genomics[9], Michael Bamshad[10,11,12], Deborah Nickerson[12], Margie L. Jaworski[13], Jieun Song[14], Hyuk Wan Ko[14], Daniel H. Cohn[5,15,16], Deborah Krakow[1,5,15,*] and Pavel Krejci[2,5,17]

[1]Department of Human Genetics, University of California Los Angeles, Los Angeles, CA 90095, USA, [2]Department of Biology, Faculty of Medicine, Masaryk University, 62500 Brno, Czech Republic, [3]Department of Histology and Embryology, Faculty of Medicine, Masaryk University, 62500 Brno, Czech Republic, [4]Central European Institute of Technology, Masaryk University, Kamenice 753/5, 62500 Brno, Czech Republic, [5]Department of Orthopaedic Surgery, [6]Department of Human Genetics, [7]Department of Obstetrics and Gynecology, Orthopaedic Institute for Children, University of California Los Angeles, Los Angeles, CA 90095, USA, [8]Institute of Experimental Biology, Masaryk University, 62500 Brno, Czech Republic, [9]University of Washington Center for Mendelian Genomics, University of Washington, Seattle, WA 98195, USA, [10]Division of Genetic Medicine, Department of Pediatrics, University of Washington, Seattle, WA 98195, USA, [11]Division of Genetic Medicine, Seattle Children's Hospital, Seattle, WA 98105, USA, [12]Department of Genome Sciences, University of Washington, Seattle, WA 98195, USA, [13]Virginia Commonwealth University, Richmond, VA 23298, USA, [14]College of Pharmacy, Dongguk University-Seoul, Goyang 410-820, Korea, [15]International Skeletal Dysplasia Registry, University of California Los Angeles, Los Angeles, CA 90095, USA, [16]Department of Molecular, Cell and Developmental Biology, University of California Los Angeles, Los Angeles, CA 90095, USA and [17]International Clinical Research Center, St. Anne's University Hospital, 65691 Brno, Czech Republic

*To whom correspondence should be addressed at: Deborah Krakow, David Geffen School of Medicine, BSRB, 615 Charles E. Young Drive S, Room 410, Los Angeles, CA 90095, USA. Email: DKrakow@mednet.ucla.edu

Abstract

The short rib polydactyly syndromes (SRPS) are a group of recessively inherited, perinatal-lethal skeletal disorders primarily characterized by short ribs, shortened long bones, varying types of polydactyly and concomitant visceral abnormalities.

†The authors wish it to be known that, in their opinion, the first two authors should be regarded as joint First Authors.

Received: June 27, 2016. **Revised:** June 27, 2016. **Accepted:** June 29, 2016

Mutations in several genes affecting cilia function cause SRPS, revealing a role for cilia function in skeletal development. To identify additional SRPS genes and discover novel ciliary molecules required for normal skeletogenesis, we performed exome sequencing in a cohort of patients and identified homozygosity for a missense mutation, p.E80K, in *Intestinal Cell Kinase*, *ICK*, in one SRPS family. The p.E80K mutation abolished serine/threonine kinase activity, resulting in altered ICK subcellular and ciliary localization, increased cilia length, aberrant cartilage growth plate structure, defective Hedgehog and altered ERK signalling. These data identify *ICK* as an SRPS-associated gene and reveal that abnormalities in signalling pathways contribute to defective skeletogenesis.

Introduction

Mammalian skeletal development is a carefully orchestrated and precisely-timed sequence of events that includes embryonic limb bud initiation and outgrowth, mesenchymal specification and condensation, cartilage differentiation and bone ossification, and finally, postnatal growth and maintenance (1). This complex process is regulated by a variety of integrated molecular mechanisms, many of which have been revealed by identifying the genes associated with skeletal dysplasia phenotypes. In many instances unappreciated components not previously known to be important to skeletogenesis have been identified, providing valuable insights into the underlying biology of skeletal development.

The short rib polydactyly syndromes (SRPS or short-rib thoracic syndromes, SRTD, MIM 208500) are a group of autosomal recessive, perinatal-lethal disorders that present with profound effects on the skeleton that include a long narrow thorax, shortened and hypoplastic long bones, and polydactyly. Other organs are also frequently affected, including the brain, heart, kidneys, pancreas, intestines and genitalia. Based on clinical and radiographic phenotypes, SRPS have historically been subdivided into types I through IV but as the associated genes are identified, the nomenclature has continued to evolve (2). SRPS share genetic and phenotypic features with other established skeletal ciliopathies, including asphyxiating thoracic dystrophy (Jeune syndrome), Ellis-van Creveld dysplasia, and Sensenbrenner syndrome, consistent with the notion that these phenotypes constitute a continuous spectrum of disease (3). Genetic studies demonstrating allelic heterogeneity among these disorders support this concept.

SRPS are caused by mutations in genes involved in the function of primary cilia, microtubule-based projections on the surface of nearly every cell that receive and integrate signalling inputs. Primary cilium function depends on intraflagellar transport (IFT), the bi-directional transport system that shuttles ciliary components, such as the tubulin building blocks, receptors, and signalling components, into and out of this organelle. The IFT machinery is composed of two distinct complexes: the kinesin-2-driven anterograde IFT-B complex, which moves components from the ciliary base to the tip, and the dynein-2-driven retrograde IFT-A complex, which transports components from the tip to the base. Mutations in genes encoding IFT-A and IFT-B components cause SRPS, including: *IFT80* (MIM 611263) (4,5), *WDR19* (MIM 614376) (6), *WDR34* (MIM 615633) (7,8), *WDR35* (MIM 614091) (9,10), *IFT140* (MIM 266920) (11,12), *IFT172* (MIM 615630) (13), *WDR60* (MIM 615462) (14), *TTC21B* (MIM 612014) (15), *DYNC2H1* (MIM 603297) (16,17), *DYNC2LI1*(18), CEP120 (19), KIAA0586 (20,21).

ICK is a MAP-like kinase belonging to the ancient yet poorly understood family of the tyrosine kinase gene *v-ros* cross-hybridizing kinase (RCK) serine-threonine kinases. The RCK kinases, which include male germ-cell associated kinase (MAK) and MAPK/MAK/MRK-overlapping kinase (MOK), are highly conserved and have been implicated in cilia biology. *ICK* was first localized in the intestinal crypt, where it regulates proliferation by promoting G1 cell cycle proliferation (22), and has since been shown to be ubiquitously expressed. ICK is a substrate of cell cycle-related kinase (CCRK), a negative regulator of ciliogenesis and cilia length (23), and ICK homologs in *Caenorhabditis elegans* (dyf-5) (24), *Chlamydomonas reinhardtii* (LF4p) (25), and *Leishmania mexicana* (LmxMPK9) (26), are also negative regulators of cilia length (24). Loss-of-function mutations in *ICK*, p.R272Q and p.G120C, cause endocrine-cerebro-osteodysplasia (ECO) (MIM 612651) an autosomal recessive, neonatal-lethal disorder similar to SRPS (27,28). Two recently characterized *ICK*-knockout mouse models recapitulate several phenotypic findings in ECO syndrome and show findings similar to SRPS that include polydactyly, shortened long bones, and an underdeveloped skeleton (29,30). In this study, we identify and characterize a novel inactivating mutation in *ICK* that produces SRPS and disrupts the architecture of the cartilage growth plate, alters hedgehog signalling, and further expands our understanding of the underlying biology that produces SRPS.

Results

Homozygosity for an inactivating mutation in *ICK* produces SRPS

To identify additional SRPS genes, exome sequencing was carried out under an approved human subjects protocol in a cohort of SRPS cases. In one individual (International Skeletal Dysplasia Registry reference number R05-024A, Figure 1A) we identified homozygosity for a point mutation, c.238G > A (NM_014920), predicting the amino acid substitution p.E80K in *Intestinal Cell Kinase* (*ICK*). The affected male was initially identified by prenatal ultrasound with features of a severe skeletal dysplasia associated with multiple congenital abnormalities, including hydrocephalus, genital abnormalities and craniofacial dysmorphism, and delivered at 38 wks gestation. He was intubated for respiratory insufficiency but succumbed within a few hours after birth. Radiographs showed a long narrow thorax with short ribs, elongated clavicles, rhizomelia, mesomelia with bending, a hypoplastic ileum and polydactyly (Figure 1B–D, Table 1) findings consistent with SRPS. Homozygosity for a different *ICK* missense mutation was characterized in the original case of ECO (27), demonstrating that these are allelic phenotypes.

ICK residue E80 lies within the highly conserved serine/threonine kinase domain and forms a direct bond with ATP as visualized by structural modelling (Figure 2A and B). *In silico* substitution of the negatively charged E80 for the positively charged K80 disrupts the electrostatic potential at the ICK-ATP interface, likely compromising ATP-binding (Figure 2B) and kinase activity. To test this prediction, we performed an *in vitro* cell-free kinase assay using purified ICK^{WT} or ICK^{E80K} and myelin basic protein (MBP) as the substrate. Phosphorylation of MBP

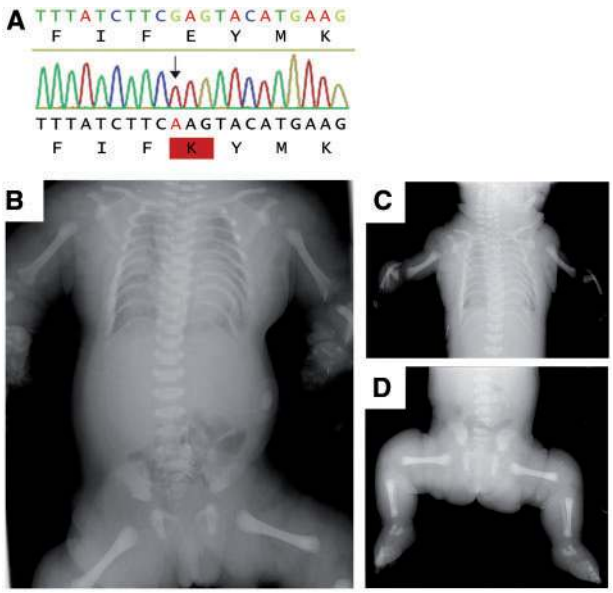

Figure 1. Homozygosity for a p.E80K substitution in *ICK* causes SRPS. (**A**). Chromatogram showing homozygosity for c.238G > A, predicting the amino acid substitution p.E80K in patient R05-024A. (**B–D**). Radiographs of R05-024A showing a long narrow chest with short ribs, elongated clavicles, shortened humeri and femora, bowed and bent radii, ulnae, tibiae, fibulae, and four limb post-axial polydactyly.

Table 1 Summary of Phenotypic Findings

Clinical Findings	R05-024
Gestational Age at Delivery (weeks)	38
Prenatal Findings	Hydrocephaly
Birth weight (grams)	4050
Birth Length (cm)	44 *cm*
Apgar Scores	2,6,7
Calvarium	Large anterior fontanel, 7 X 7 cm, widely split sutures,frontal bossing
Eyes	Small palpebral fissures, fused eyelids
Nose	Short, upturned with tented alae
Mouth	Microstomia
Ears	Low set, posteriorly rotated, poorly formed with absent anti-helix formation
Neck	Short
Thorax	Long, narrowhorizontal ribs with some bendingRelative long appearing clavicles
Genitalia	External genital absent
Gastrointestinal	Anus present
Renal	No abnormalities detected
Upper extremities	Foreshortened humeri bowed and bent radii and ulnae, smooth metaphyseal ends of the long bones, postaxial polydactyly
Pelvis	Long narrow ileum, smooth acetabular roof, high ischia
Lower extremities	Shortened femora, bowed and bent tibia and femora, smooth metaphyseal ends of the long bones, postaxial polydactyly

was achieved with ICK^{WT} but not with ICK^{E80K}, indicating that the p.E80K substitution abrogates kinase activity (Figure 2C).

Having established that ICK^{E80K} is kinase-dead, we next asked if this would prevent activation of the protein. Activation of ICK is regulated by dual-phosphorylation of its T^{157}-D-Y^{159} motif: auto-phosphorylation of Tyr^{159} achieves basal activation and CCRK-mediated phosphorylation of Thr^{157} achieves full activation (31). Because Tyr^{159} phosphorylation reflects the basal ICK activity, it can be used as a surrogate to estimate the levels of ICK activation (32). Figure 2D shows that ICK^{E80K} was unable to auto-phosphorylate at Tyr^{159}, while ICK^{R272Q} found in ECO syndrome (27) retained approximately one third of Tyr^{159} phosphorylation compared to ICK^{WT}. We conclude that p.E80K is a loss-of-function mutation differing from ICK^{R272Q}.

ICK^{E80K} demonstrates altered subcellular localization

Previous studies have established that ICK functions as both a cytoplasmic and nuclear kinase, suggesting that it shuttles between these two compartments (27,32,33). Immunohistochemistry performed on HEK293T cells revealed significant differences between ICK^{WT} and ICK^{E80K} localization (Figure 3A). While ICK^{WT} localized evenly between the nucleus and cytosol, ICK^{E80K} localized predominantly, but not exclusively, to the nucleus. The ECO mutant ICK^{R272Q} was almost exclusively cytosolic as described before (27,32) (Figure 3B). Although we do not know the reason for this difference, it is important to note that different residues are mutated, the substituted amino acids have different charge consequences, and the ECO mutation only partially impaired ICK activity when compared to the total loss of function mutation p.E80K (Figure 2C and D). Interestingly, Arg^{272} is a part of the conserved ^{269}PKKRP^{273} motif which serves as a nuclear localization sequence (NLS) necessary for tagging ICK for nuclear import (32).

ICK kinase activity regulates ciliogenesis and ciliary localization

To investigate ICK function during ciliogenesis, we expressed ICK^{WT}, ICK^{E80K} and ICK^{R272Q} in NIH3T3 mouse embryonic fibroblasts. Overexpression of ICK^{WT} inhibited cilia formation in these cells, similar to recently published data (29). By contrast, weaker overexpression of ICK^{WT} inhibited ciliogenesis to a lesser degree, suggesting that the level of ICK activity correlates inversely with ciliogenesis (Figure 4A–C). While strong overexpression of ICK^{E80K} inhibited ciliogenesis, weaker overexpression of ICK^{E80K} did not, suggesting that the kinase activity of ICK is required to negatively regulate ciliogenesis. In line with that, cells weakly overexpressing partially inactive ICK^{R272Q} formed cilia with frequency between ICK^{WT} and ICK^{E80K} (Figure 4A). We also observed that cells expressing ICK^{WT} had shorter cilia than controls, and that expression of ICK^{E80K} produced longer cilia as compared with both the ICK^{WT}- or ICK^{R272Q} -transfected cells and the control (Figure 4G). The cilia in the ICK^{E80K} mutant cells were longer, with greater variability in length, than in ICK^{WT} cells, suggesting that ICK kinase activity correlates inversely with the cilia length (Figure 4G). Concordant with these findings, longer cilia were also observed in cultured cells lacking ICK due to RNAi knockdown or in cells from the *Ick* knockout mouse (29). Localization within the cilia also differed between the ICK variants; ICK^{E80K} and ICK^{R272Q} predominantly localized to the tip of the cilia compared with ICK^{WT}, which localized almost exclusively to the cilia base (Figure 4D and E). Interestingly, only a minority of ICK^{R272Q}-transfected cells localized the transgenic ICK to cilia, which was in contrast with ICK^{WT} and ICK^{E80K} cells where the majority of cilia were positive for ICK (Figure 4F). R272Q thus impairs ICK ability to localize to both the nucleus and cilia. Altogether, the loss of kinase activity in ICK^{E80K} altered

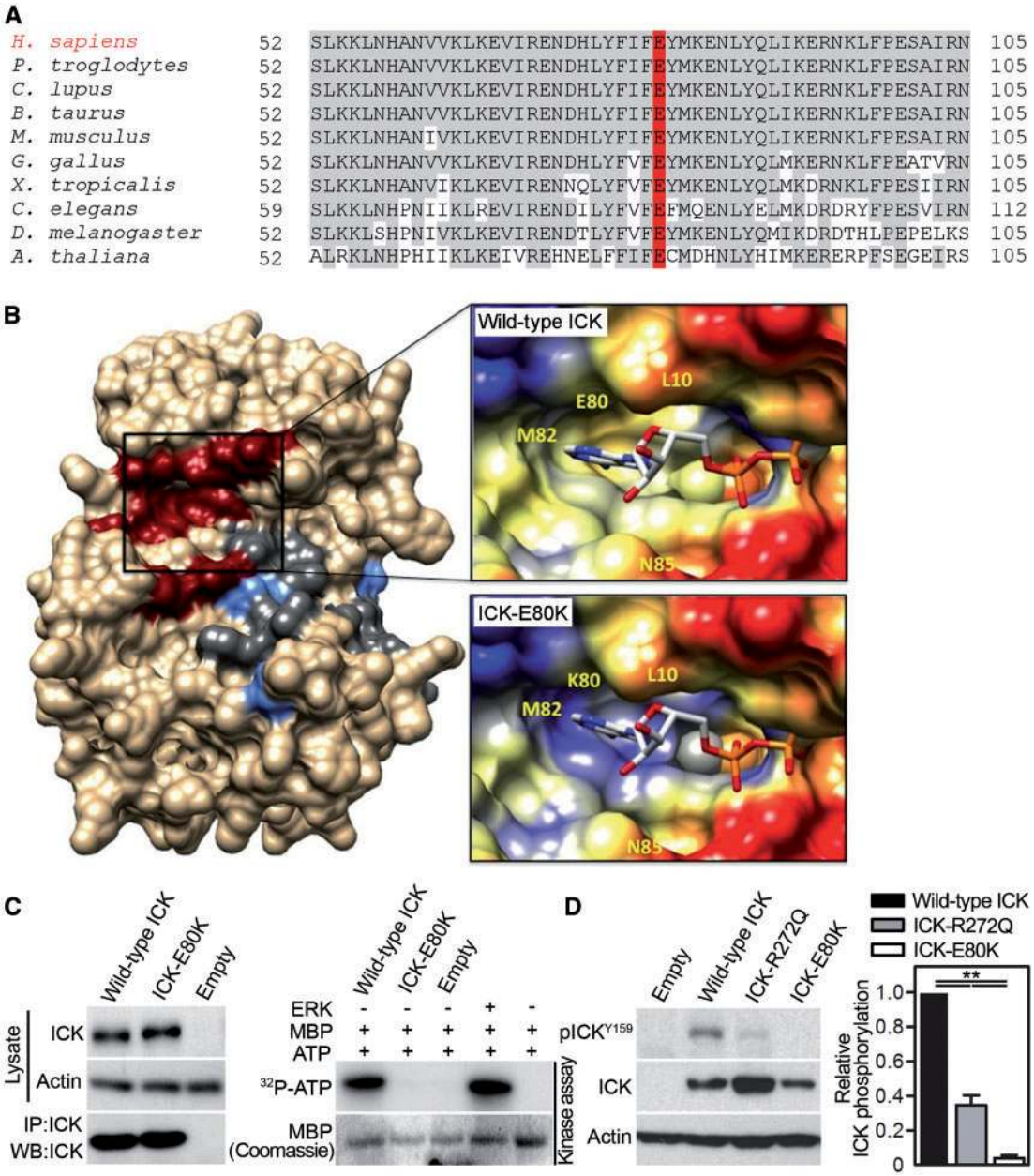

Figure 2. p.E80K mutation abrogates ICK kinase activity. (**A**). Alignment of *ICK* homologs demonstrates conservation of residue E80. Conserved residues among ICK homologs are shaded in grey; E80 is highlighted in red. (**B**). 3D model of the catalytic domain of ICK. ATP-binding site (red), substrate-binding site (blue), and activation loop (grey). Substitution of the negatively charged glutamic acid (red) for the positively charged lysine (blue) at residue 80 is predicted to alter the electrostatic potential at the ICK-ATP interface (lower right inset), suggesting abolition of ATP-binding. (**C**). HEK293T cells were transfected with empty vector (control), wild type ICK (ICK^{WT}), or mutant ICK (ICK^{E80K}) as indicated and the FLAG-tagged ICK proteins were purified by FLAG immunoprecipitation (IP). Kinase activity was measured *in vitro* using myelin basic protein (MBP) as substrate in the presence of [^{32}P]-ATP. Phosphorylation of MBP by recombinant ERK2 (ERK) served as a positive control for the kinase assay. The ICK^{E80K} reaction shows complete loss of kinase activity as measured by ^{32}P incorporation. (**D**). HEK293T cells transfected with either ICK^{WT}, ICK^{R272Q} or kinase-dead ICK^{E80K} were analyzed for ICK activation as measured by phosphorylation of Tyr^{159} (belonging to the activation T^{157}-D-Y^{159} motif). Mutant ICK^{E80K} had only minimal activity, while ICK^{R272Q} retained approximately a third of Tyr^{159} phosphorylation compared to ICK^{WT} (right panel; normalized to ICK expression levels). (Student's t-test, $^{**}P<0.01$; $n=3$).

its subcellular localization, ciliogenesis, cilia length, and distribution within primary cilia.

Cilia from R05-024A fibroblasts are long and twisted

We further addressed the ciliary architecture in patient-derived fibroblasts. R05-024A fibroblasts produced longer cilia, on average, compared to control fibroblasts (Figure 5A–C) in agreement with the ICK expression studies in NIH3T3 cells (Figure 4G). Scanning electron microscopy analysis showed that cilia from R05-024A fibroblasts appeared thin and twisted as compared control fibroblast cilia (Figure 5D). The evidence obtained from both R05-024A primary fibroblasts and ectopic expression studies in NIH3T3 cells demonstrated that kinase-inactive ICK^{E80K} produced elongated cilia in agreement with previous studies on *ICK* mutations (29,34).

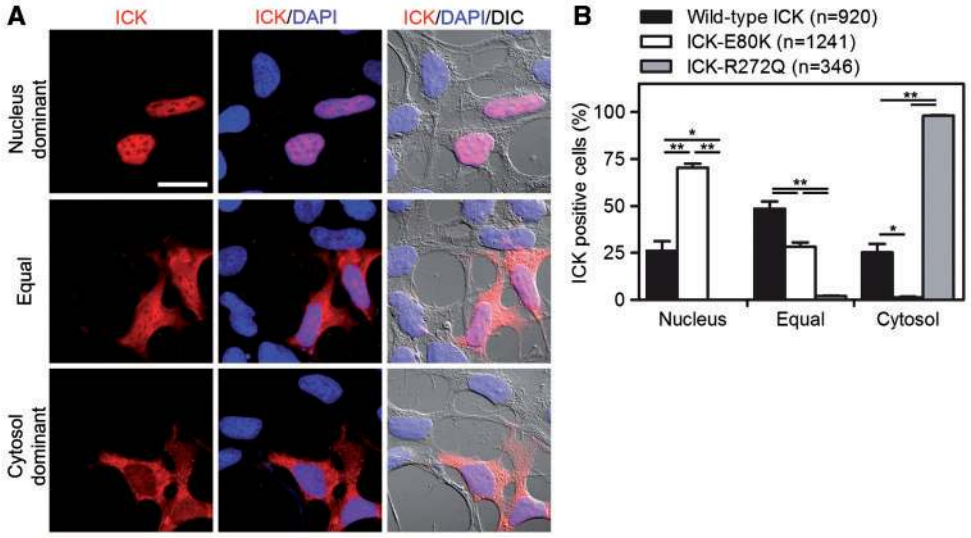

Figure 3. The p.E80K substitution alters ICK subcellular localization in HEK293T cells. ICK overexpression resulted in typical localization patterns shown in (A) (scale bar, 10 μm) (DIC, differential interference contrast). (**B**). Immunohistochemistry in HEK293T revealed differences in localization between ICK^{WT} (nuclear and cytosolic), ICK^{E80K} (primarily nuclear) and ICK^{R272Q} (almost exclusively cytosolic). (Student's t-test, $^{*}P< 0.05$, $^{**}P< 0.01$).

Impaired GLI3 processing and Hedgehog (Hh) signalling in R05-024A fibroblasts

To investigate whether the *ICK* mutation impaired Hh signalling, we stimulated fibroblasts from R05-024A and controls with smoothened agonist (SAG) (35) and quantified the resulting amounts of GLI3 full-length (GLI3FL) and repressor (GLI3R) forms as readout for GLI3 activity. In the absence of pathway stimulation, GLI3FL was normally processed into GLI3R, as demonstrated in control fibroblasts (Figure 6A). R05-024A fibroblasts demonstrated a higher baseline ratio of GLI3FL to GLI3R amounts as compared with control fibroblasts (Figure 6A). With SAG stimulation, control fibroblasts demonstrated an increased GLI3FL to GLI3R ratio, indicative of pathway activation, yet in R05-024A fibroblasts there were negligible changes in this ratio upon SAG treatment. In R05-024A fibroblasts, there was markedly less GLI3R relative to GLI3FL and GLI3 activated processing was impaired, suggesting that mutant ICK altered GLI3 activity. To investigate this further, we visualized ciliary localized GLI3 and found that endogenous GLI3 accumulated to a far greater extent in primary cilia tips in R05-024A relative to control fibroblasts (Figure 6B). In addition, GLI3 accumulation in R05-024A cilia persisted longer after exposure to SAG when compared with control cells, which showed similar GLI3 levels with no accumulation over time, consistent with impaired GLI3 processing due to the ICK^{E80K} mutation (Figure 6B). To see whether impaired GLI3 processing lead to altered expression of Hh target genes, we analyzed levels of *GLI1* and *PTCH1* transcripts. Compared to control fibroblasts, the R05-024A cells showed higher basal levels of *GLI1* and *PTCH1* expression (Figure 6C), which corresponds to less abundant repressor GLI3 (GLI3R) in these cells (Figure 6A). Treatment with SAG resulted in significantly lower induction of *GLI1* and *PTCH1* expression in R05-024A, altogether demonstrating a defective response to Hh signal (Figure 6D).

Ick$^{-/-}$ mouse cartilage growth plates show abnormalities in architecture and impaired Hh signalling

Because of the profound effect of ICK mutations on skeletal development in humans and mice, we investigated the localization of ICK in the distal femoral cartilage growth plate of P1 WT mice. Histologic analyses performed with ICK antibody showed ubiquitous ICK expression, with particularly higher expression in the proliferating and prehypertrophic zone chondrocytes, and relatively less expression in hypertrophic chondrocytes (Supplementary Material, Fig. S1). Minimal expression was seen in the perichondrium and primary spongiosum (Supplementary Material, Fig. S1). Similar to previous findings in transfected cells, the intracellular distribution of ICK was both cytoplasmic and nuclear (Supplementary Material, Fig. S1). Because the cartilage growth plate from case R05-024A was not available, we examined growth plate cartilages of the *Ick*$^{-/-}$ animals (29). Picrosirius red staining of the control and *Ick*$^{-/-}$ growth plates revealed marked disruption of growth plate architecture, with a shortened proliferative zone and poor column formation in the hypertrophic zone, with fewer cells contributing to the hypertrophic chondrocyte columns in *Ick*$^{-/-}$ compared to *Ick*$^{+/-}$ growth plates (Figure 7A and B). In addition, proliferating and hypertrophic chondrocytes were subjectively smaller with less cytoplasm and diminished extracellular matrix between cells, leading to the appearance of increased cellularity throughout the growth plate (Figure 7A and B). The primary spongiosum also showed diminished numbers of discrete trabeculae (Figure 7A and B) and, similar to the radiographs in the affected neonate and the *Ick*$^{-/-}$ skeletal preparations (29), there was bending at the mid-diaphyseal portion of the humeral bone (Figure 7A), as well as other bones in the appendicular skeleton (data not shown). The proliferative and hypertrophic zone alterations suggest defects in both cellular proliferation and chondrocyte differentiation, and the hypercellularity may result from an effect on extracellular matrix synthesis due to loss of *Ick*.

Ihh is a well-recognized morphogenic organizer of the growth plate cartilage, which is produced by a narrow zone of early hyperthrophic chondrocytes and is critical for proper chondrocyte progression from proliferating to hypertrophic stages (36). The *in situ* hybridization analysis of *Ihh* expression in the growth plates of E18.5 *Ick*$^{-/-}$ embryos showed a normal distribution when compared to *Ick*$^{+/-}$ (Figure 7C). This contrasted *Gli1* and *Ptch1* expression, which was virtually absent in

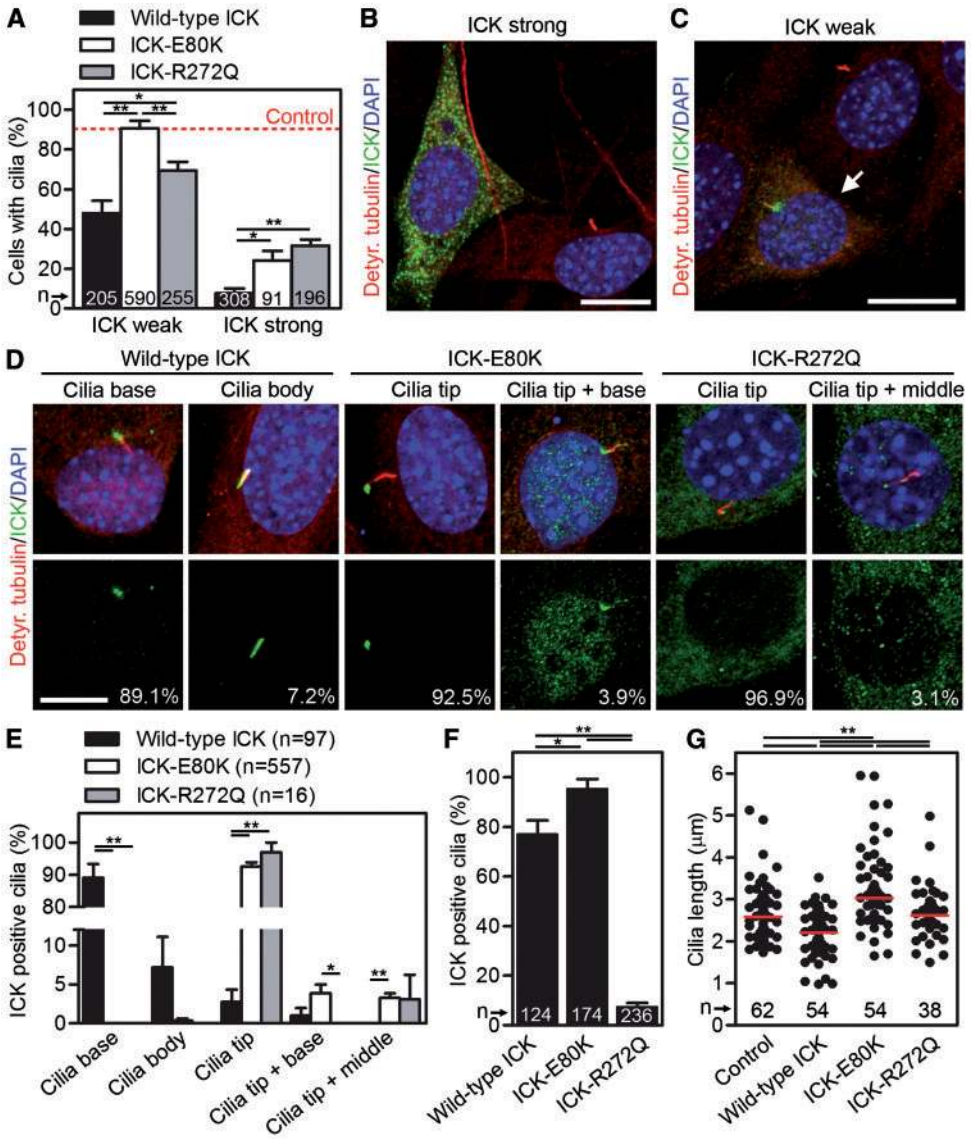

Figure 4. p.E80K substitution alters ICK distribution in primary cilia. (**A-G**). NIH3T3 cells were transfected with FLAG-tagged ICK^{WT}, ICK^{E80K} or ICK^{R272Q} and starved for 24 h. (**A**). Ectopic ICK expression reduced ciliogenesis compared to non-transfected controls, with the most pronounced reduction in ICK^{WT} cells (Student's t-test, *P< 0.05, **P< 0.01). (**B**). Cells that strongly overexpressed ICK typically lack primary cilia, compared to cells with weak ICK expression, (**C**) (arrow). (**D**). FLAG-ICK^{WT} primarily localized to the ciliary base. FLAG-ICK^{E80K} and -ICK^{R272Q}, in contrast, primarily localized to the ciliary tip. (**E**). Quantification of ICK localization demonstrates differences between ICK^{WT}, ICK^{E80K} and ICK^{R272Q} (t-test, *P< 0.05, **P< 0.01). (**F**). Most of the cells localized FLAG-ICK^{WT} and -ICK^{E80K} to cilia, but only minority of cilia was positive for FLAG-ICK^{R272Q} (Student's t-test, *P< 0.05, **P< 0.01). (**G**). ICK^{WT} transfection shortened, while ICK^{E80K} elongated cilia compared with control NIH3T3 cells (t-test, **P< 0.01). Dots indicate individual cilia, red bars indicate medians. Scale bars, 10 µm.

proliferating chondrocytes and adjacent perichondrium in the *Ick*$^{-/-}$ growth plates, demonstrating defective responsive to Ihh within the growth plate (Figure 7C).

Altered ERK MAP kinase activity in R05-024A fibroblasts and *Ick*$^{-/-}$ growth plate chondrocytes

Cartilage growth plate analyses showed a decreased number of proliferating cells and ICK was highly expressed in the proliferative zone. This suggested that ICK could be involved in the regulation of chondrocyte proliferation and differentiation. Because it has been well established that elevated ERK activation inhibits chondrocyte proliferation, induces premature senescence and disturbs chondrocyte differentiation (37,38), we tested the hypothesis that ERK activity might be altered in R05-024A cells. We found increased basal activating phosphorylation of ERK and other members of an ERK signalling module such as C-RAF and MEK in R05-024A fibroblasts compared with control cells (Figure 8A). Chemical inhibition of ERK pathway in R05-024A fibroblasts did not significantly shorten cilia, suggesting that increased ERK activity is not responsible for the long cilia seen in R05-024A fibroblasts (Figure 8B and C). We next evaluated whether a similar increase in ERK activation occurs in the growth plates of *Ick*$^{-/-}$mice. Femoral and tibial growth plates were harvested and analyzed for ERK activating phosphorylation by western blot. In contrast with the R05-024A fibroblast data, we found less ERK phosphorylation in both femurs and tibias isolated from *Ick*$^{-/-}$mice, demonstrating different ERK regulation by ICK in fibroblasts and growth plate chondrocytes (Figure 8D).

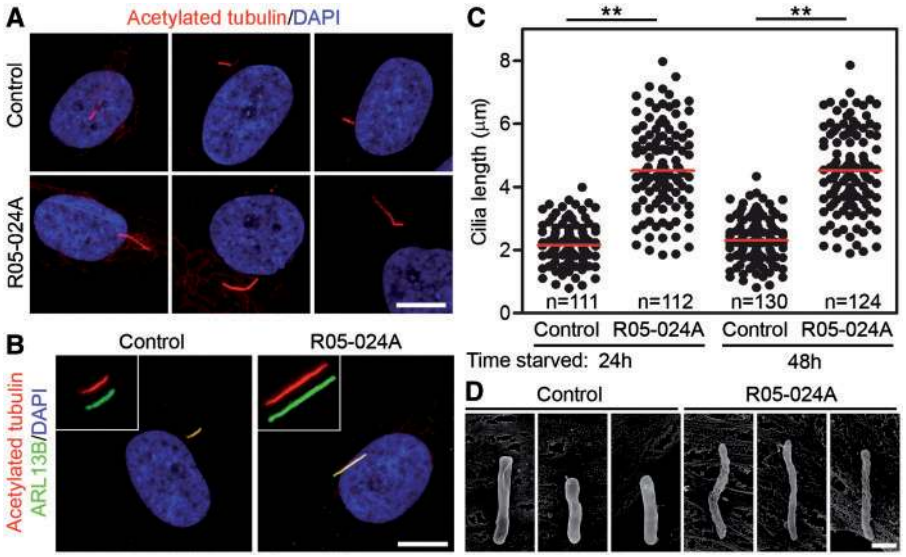

Figure 5. R05-024A fibroblasts have long cilia with abnormal morphology. (**A, B**). Control and R05-024A fibroblasts stained for the cilia markers acetylated α-tubulin (AcTub, red) or ARL13B (green) (scale bars, 5μm). (**C**). R05-024A fibroblasts produced longer cilia compared to control fibroblasts. Cilia length was measured using the AcTub staining and ImageJ software (t-test, $^{**}P < 0.01$). Dots indicate individual cilia, red bars indicate medians. (**D**). Scanning electron microscope demonstrated ultrastructural differences, with R05-024A cilia appearing long, gaunt, and twisted. Scale bar, 1μm.

Discussion

Here we show that homozygosity for a kinase-inactivating mutation in *ICK*, p.E80K, causes short rib polydactyly syndrome (SRPS). Functional characterization of the p.E80K mutation revealed total loss of kinase activity, malformed and elongated primary cilia, abnormal growth plate morphology and impaired GLI3 processing coupled with defective expression of *GLI1* and *PTCH1*. Homozygosity for a different *ICK* missense mutation, p.R272Q, produced ECO syndrome, a distinct disorder delineated in the Old Order Amish population (27). Shared phenotypic findings between the two disorders include hydrocephalus, fused eyelids, small palpebral fissures, abnormally shaped and rotated ears, genitourinary abnormalities, shortened long bones, bowing of bones in the mesomelic segment and polydactyly. Thus, the mutations in ICK can produce an allelic spectrum of disease from ECO to SRPS.

Residue E80 of ICK occurs within a highly conserved domain that is required for ATP binding; we show that the mutation of this residue abolished kinase activity, likely by destabilizing the ATP-binding pocket. We demonstrated loss of kinase activity in ICK^{E80K}; first, purified ICK^{WT}, but not ICK^{E80K}, was able to phosphorylate MBP in an *in vitro* kinase assay; second, phosphorylation of Tyr159, the site of ICK auto-phosphorylation that reflects basal activation, was detected in lysates from cells expressing ICK^{WT}, limited down to one third in ICK^{R272Q}, but was nearly absent in ICK^{E80K}. These findings suggest that the extent of ICK kinase activity influences skeletogenesis, distinguishing the phenotypic consequences between ECO and SRPS mutations.

We also showed that the kinase activity of ICK is important for both cilia structure and ciliogenesis. Both patient-derived primary fibroblasts and NIH3T3 cells expressing ICK^{E80K} produced longer cilia than their respective controls. Additionally, the cilia from patient-derived fibroblasts appeared gaunt and twisted, similar to the structures of cilia from Kif7 mutants $Kif7^{L130P}$ and $Kif7^{-/-}$ (39), suggesting that ICK may be required for ciliary structural integrity. Further, expression of ICK inhibited ciliogenesis in NIH3T3 cells in a dose-dependent manner. Notably, ICK^{WT} was a much stronger inhibitor of ciliogenesis than ICK^{R272Q}, and weakly expressed kinase-dead ICK^{E80K} did not inhibit ciliogenesis at all, suggesting that the regulation of ciliogenesis by ICK also depends on the level of kinase activity. This is supported by work showing that a form of ICK that is resistant to activation, ICK^{T157A}, is a weak suppressor of ciliogenesis when compared with ICK^{WT} (23). It is therefore likely that the loss of kinase activity underlies the ciliary phenotype in R05-024A.

Proteins destined for the cilia must enter through the ciliary gate, a structure of the transition zone between the basal body and the ciliary axoneme (40) where a sorting mechanism prevents the entry of membrane vesicles and ribosomes and guards against uncontrolled diffusion of cytosolic proteins into the cilia (41). Figure 4E shows that the majority of ICK^{WT} expressed in NIH3T3 cells localized to the basal body, whereas the majority of mutant ICK^{E80K} or ICK^{R272Q} localized to the cilia tip. A similar pattern of ICK localization was found in cells expressing ICK^{WT} or the kinase-dead mutants ICK^{K33R} and ICK^{TDY} (29). Collectively, this evidence suggests that ICK normally localizes to the basal body and this localization depends on kinase activity. In addition, the observation that ICK^{R272Q} failed to enter both nucleus and primary cilia in most cells suggests that the NLS motif disrupted by R272Q substitution also tags ICK for targeting to cilia. This resembles the situation in KIF17, where the substitution of the NLS motif by alanines disrupts targeting of KIF17 both to the nucleus and cilia (42).

In mammals, primary cilia are essential for Hh pathway signal transduction (43). In the absence of Hh stimulation, GLI3 predominates in the processed, repressor form (GLI3R). When the Hh pathway is stimulated, processing of GLI3 stops, the GLI3R form diminishes and there is increased active full length GLI3 (GLI3FL). Achieving the proper balance of GLI3FL to GLI3R is essential for digit specification and Hedgehog induced signal activity and requires IFT-mediated trafficking through the primary cilium (44). Imbalance of GLI3FL to GLI3R resulting from deficient IFT underlies the polydactyly seen in many ciliopathies (18). Our finding of impaired GLI3 processing, the resulting increased GLI3FL to GLI3R ratio and impaired *GLI1* and *PTCH1* expression in R05-024A fibroblasts is consistent with previous studies of other cilia and IFT

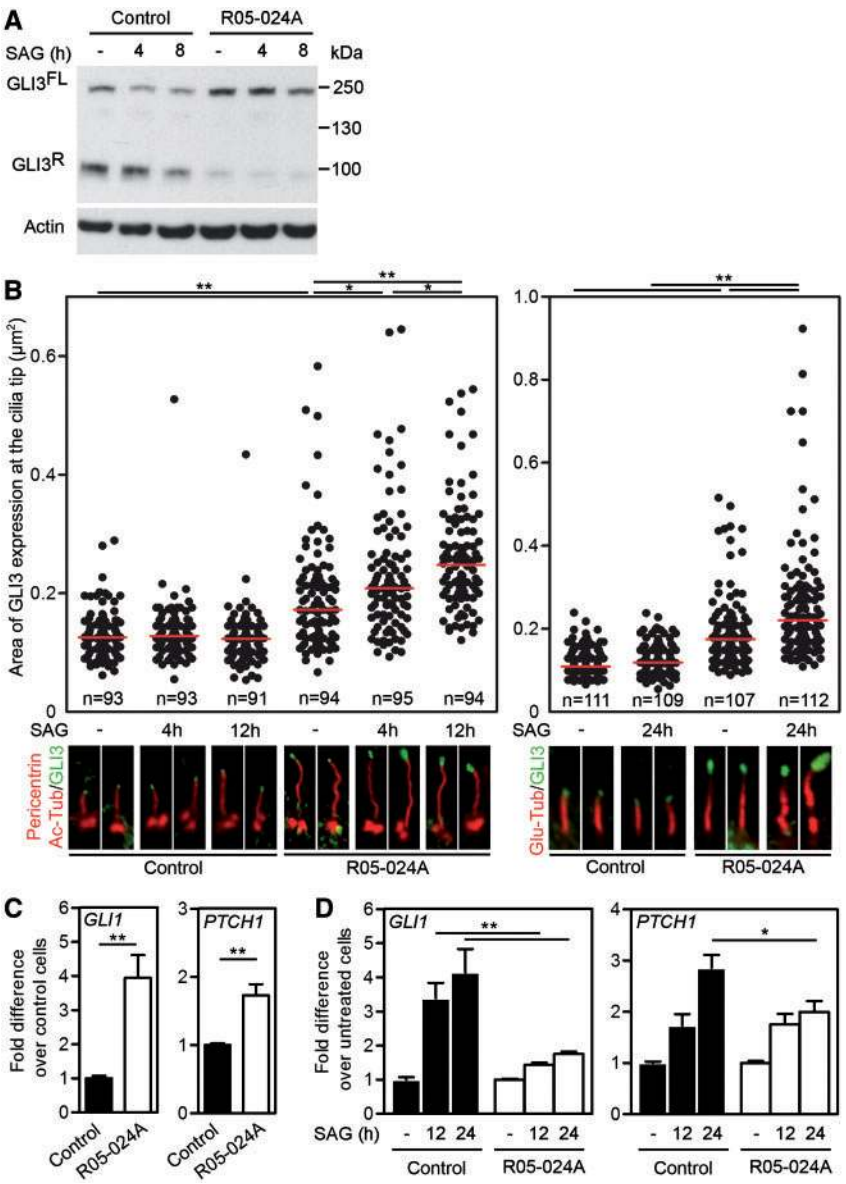

Figure 6. R05-024A fibroblasts are deficient at processing and trafficking GLI3, and transactivation of *GLI1* and *PTCH1* expression. (**A**). Lysates from R05-024A fibroblasts showed an increased ratio of full-length ($GLI3^{FL}$) to repressor ($GLI3^{R}$) GLI3 in both the presence and absence of 500nM SAG. Actin served as a loading control. (**B**). Cilia from R05-024A fibroblasts exhibited pronounced accumulation of GLI3 at their tips. Cells were treated with either 500nM (4 and 12 h) or 100nM (24 h) SAG, and stained for GLI3, pericentrin, acetylated α-tubulin (Ac-Tub) or polyglutamylated tubulin (Glu-Tub). The areas of GLI3 signal at the cilia tips were quantified and plotted using ImageJ software. Dots represent individual GLI3 areas, red bars indicate medians. (t-test, $^{*}P< 0.05$, $^{**}P< 0.01$). (**C**). R05-024A fibroblasts have elevated levels of basal *GLI1* and *PTCH1* expression (t-test, $^{**}P< 0.01$; $n = 4$). (**D**). Treatment with 500 nM SAG induces *GLI1* and *PTCH1*, that is reduced in R05-024A fibroblasts compared with control cells (t-test, $^{*}P< 0.05$, $^{**}P< 0.01$; $n = 4$).

mutants: Ift88 ($Tg737^{\Delta 2\text{-}3\beta\text{-}gal}$) (45), ($Ift88^{null}$ and $Ift88^{hypo}$) (46); Sufu ($Sufu^{-/-}$) (47); C2cd3 (*Hty*) (48); Dync2h1 ($Dnchc2^{lln}$) (49); Ptch1 (45); Ift172 (49); Kif3a (49); Fuz (50); Ift122 ($Ift122^{-/-}$) (51); $IFT52^{hypo}$ (46); $Kif7^{-/-}$ (52–54). Similar to other genes responsible for cilia function, in the ICK^{E80K} mutant, the imbalance in GLI3FL to GLI3R appears to underlie the polydactyly in R05-024A.

Concomitant to impaired GLI3 processing, the area of ciliary GLI3 accumulation in R05-024A fibroblasts was greater than that of controls, and this observation was exaggerated by SAG treatment. The progressive, SAG-mediated accumulation of GLI3 at the ciliary tips of R05-024A fibroblasts suggests some degree of intact anterograde transport but defective unloading at the cilia tip and/or impaired GLI3 export out of the cilia. Although the exact mechanism of ICK-mediated regulation of cilia function and GLI3 processing remains to be determined, some of its features are beginning to emerge. For example, modulation of ICK activity affected the transport velocities of several IFT components, including those belonging to both anterograde IFT-B (KIF3A, IFT20) and retrograde IFT-A (IFT43) particles, resulting in their accumulation at ciliary tips in ICK-deficient cells (30,34). Interestingly, loss-of-function mutations in the *C. elegans* ICK homolog DYF-5 resulted in slower IFT and impaired docking and undocking of kinesin motors from IFT particles (24). It is therefore possible that slow IFT and/or impaired undocking of cargo causes GLI3 accumulation at the tips of R05-024A cilia (55).

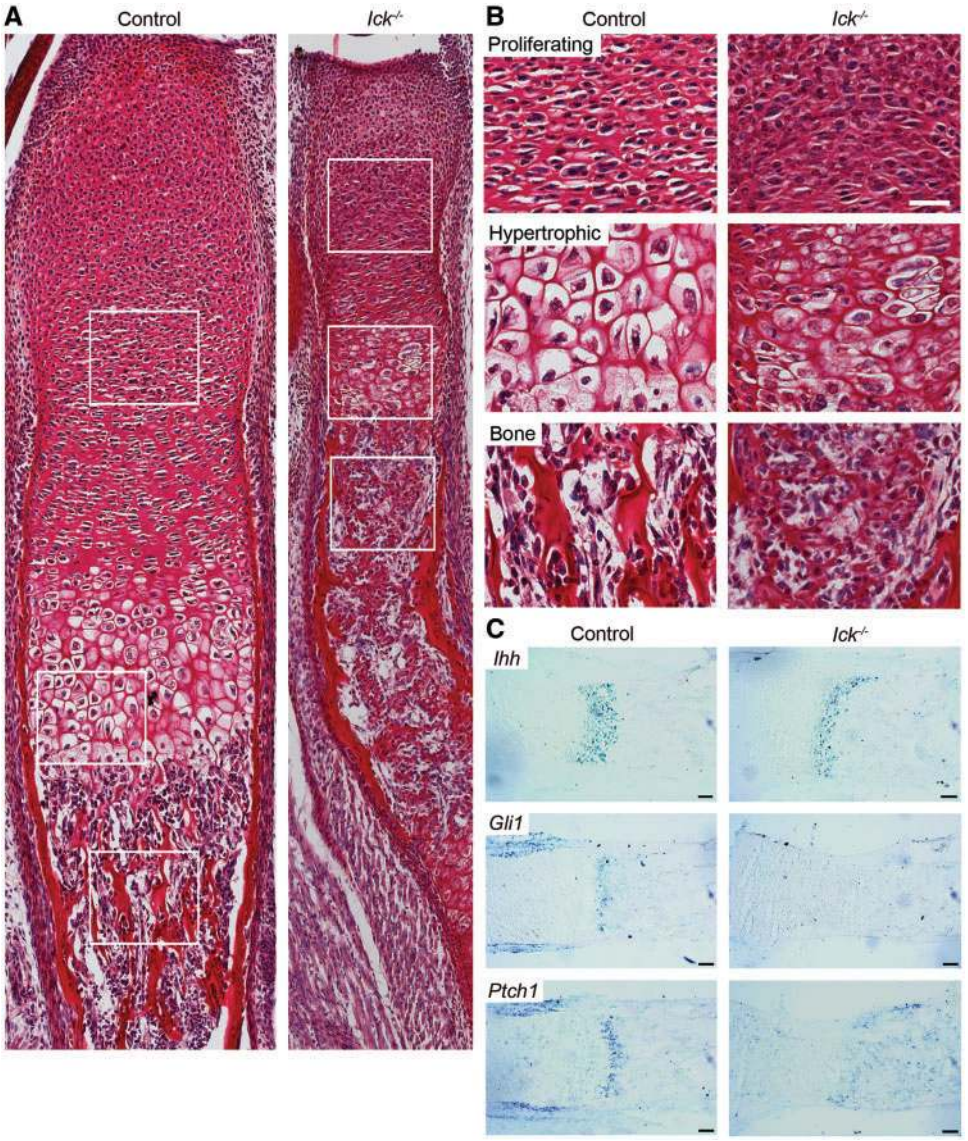

Figure 7. Growth plates of *Ick*$^{-/-}$ mouse have abnormal architecture and diminished *Gli1* and *Ptch1* expression. Histological analysis of control and *Ick*$^{-/-}$ mouse growth plates. (**A**). Picrosirius red staining of markedly short and hypoplastic *Ick*$^{-/-}$ humeral growth plate cartilage compared to normal control. (**B**). Comparative sections of proliferating cartilage, hypertrophic cartilage and primary bone delineated by white squares in (**A**). Note shortening of the proliferative zone, loss and disorganization of columnar hypertrophic chondrocytes, smaller appearing proliferative and hypertrophic chondrocytes, subjectively increased cellularity throughout the growth plate, and diminished trabeculae in the primary spongiosum in *Ick*$^{-/-}$ growth plates. Scale bar, 50 μm. (**C**). RNA *in situ* hybridization analysis of the proximal tibial growth plates obtained from E18.5 control and *Ick*$^{-/-}$ mice. While *Ihh* expression does not differ significantly between *Ick*$^{-/-}$ and control, the expression of *Ihh* target genes *Gli1* and *Ptch1* is eliminated from the *Ick*$^{-/-}$ growth plates or adjacent perichondrium, suggesting a defective chondrocyte response to Ihh stimulus. Scale bars, 40 μm.

While we have shown that homozygosity for a mutation *ICK* produces a SRPS, little is known regarding the expression of this gene in the developing skeleton. Immunohistochemistry of a newborn mouse femur demonstrated robust expression of ICK throughout the growth plate as well as in the periosteum/perichondrium and the primary spongiosum. Strong expression was seen in reserve and proliferating chondrocytes and its zone of expression was more extensive than that of Indian hedgehog (IHH), for which expression is primarily in pre-hypertrophic and early hypertrophic chondrocytes (36). Altered GLI3 processing would be predicted to have downstream consequences in the cartilage growth plate IHH signalling. This hypothesis was confirmed by the lack of expression of IHH targets *Gli1* and *Ptch1* in the growth plates of the *Ick*$^{-/-}$ mouse.

Although we could not examine the histological appearance of R05-024A growth plate cartilage, the growth plate defects in *Ick*$^{-/-}$ animals shared some resemblance to those seen in thanatophoric dysplasia (TD), including a short proliferative zone, small proliferating and hypertrophic chondrocytes, and decreased extracellular matrix (Figure 7A and B) (56), suggesting that the two disorders might share some underlying mechanism. Mutated FGFR3 causes TD via aberrant activation of ERK MAP kinase, which inhibits chondrocyte proliferation, induces premature senescence and disturbs chondrocyte differentiation, leading to a short and disorganized cartilage growth plate cartilage (37,38). In intestinal epithelial cells, suppression of ICK expression via RNA interference results in growth arrest in the G1 phase of the cell cycle, accompanied with induction of

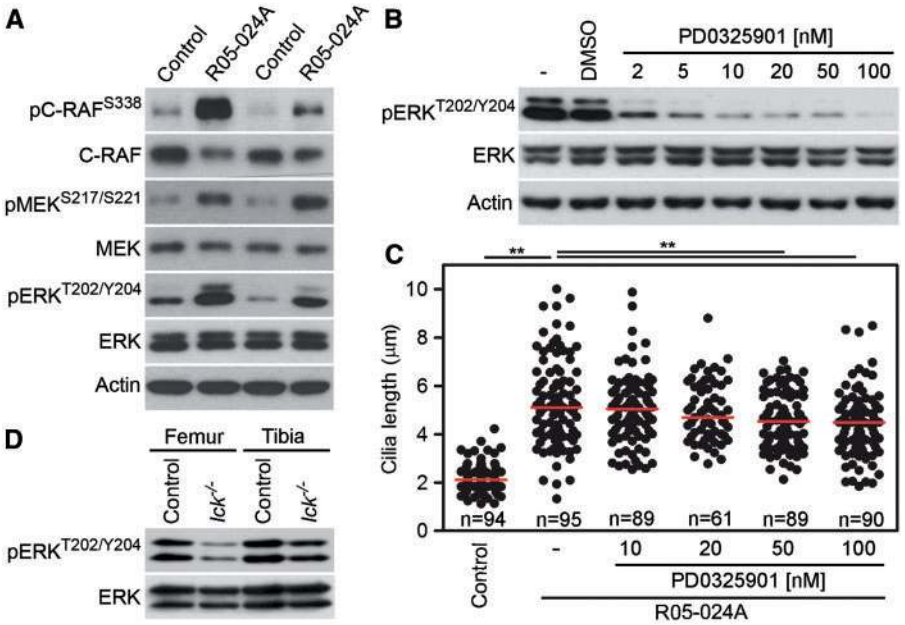

Figure 8. Modulation of ERK MAP kinase activity by ICK (**A**). R05-024A fibroblasts accumulated phosphorylated (p) ERK or upstream members of its signalling module (MEK and C-RAF kinases) as compared with control fibroblasts. (**B-C**). Inhibition of ERK pathway with chemical inhibitor (PD0325901) did not affect the cilia elongation phenotype in R05-024A fibroblasts (compared to control fibroblasts, Student's t-test, $^{**}P < 0.01$). Dots represent individual cilia, red bars indicate medians. (**D**). ERK MAP kinase activity in *Ick*$^{-/-}$ mice was reduced. Western blot analysis of femoral or tibial bone from *Ick*$^{-/-}$ mutant and control littermate (P0) was performed to measure the ERK kinase activity. The antibodies recognized the phosphorylated ERK (pERK$^{T202/Y204}$) or total ERK (ERK) from femoral or tibial protein extracts and showed that the relative level of pERK was reduced in mutant compared with wildtype control.

p21$^{Cip1/WAF1}$ cell cycle inhibitor (22). Similar changes accompany FGFR3/ERK-mediated growth arrest in chondrocytes (57), suggesting the possibility that kinase inactive ICK-E80K causes SPRS in part via ERK-mediated inhibition of chondrocyte proliferation. Interestingly, we found increased basal ERK activation in R05-024A patient fibroblasts compared to control cells. These data were, however, in contrast to the similar analysis carried-out in the growth plates of *Ick*$^{-/-}$ animals, which showed decreased ERK phosphorylation when compared to control growth plates (Figure 8D). As ERK regulates terminal chondrocyte differentiation (58), the lower ERK activation in *Ick*$^{-/-}$ samples might be explained by the lack of the hypertrophic chondrocytes in the *Ick*$^{-/-}$ growth plates. Future experiments should aim on elucidation of the precise role of ERK in ICK signalling in the growth plate cartilage.

Our findings that a mutation in ICK produces a form of SRPS adds to the growing number of genes that when mutated produce this disorder. Many of the previously identified genes are components of the ciliary IFT machinery, while ICK is a serine-threonine kinase. Another gene that is responsible for SRPS is NEK1 (59), a member of the NIMA related kinases in mammals that regulates ciliogenesis (60). It also is a serine/threonine/tyrosine kinase involved in cell cycle regulation and, similar to ICK, is localized in the centrosome/basal body (61). These data contribute to an emerging theme in SRPS, suggesting that altered signalling through phosphorylation by serine/threonine kinases represent an additional cellular mechanism by which skeletal ciliopathies can be produced.

Material and Methods

Exome sequencing

Under an approved human subjects protocol, DNA was isolated and submitted to the University of Washington Center for Mendelian Genomics for library preparation and exome sequencing. The samples were barcoded, captured using the NimbleGen SeqCap EZ Exome Library v2.0 probe library targeting 36.5Mb of genome, and sequenced on the Illumina GAIIx platform with 50 bp reads. Novoalign was used to align the sequencing data to the human reference genome [NCBI build 37] and the Genome Analysis Toolkit (GATK) (62) was used for post-processing and variant calling according to GATK Best Practices recommendations (63,64). Average coverage of targeted bases was 49X with 91% of targeted bases covered by at least 10 independent reads. Variants were filtered against dbSNP137, 95 NIEHS EGP exome samples (v.0.0.8), 6503 exomes from the NHLBI Exome Sequencing Project (ESP6500), 1000 genomes (release 3.20120430), and 40 in-house exome samples. Mutations were further compared with known disease-causing mutations in HGMD (2012.2). Variants were annotated using VAX (65) and mutation pathogenicity was predicted using the programs Polyphen (66), Sift (67), Condel (68), and CADD (69). The mutation reported in this work was confirmed by bidirectional Sanger sequencing of amplified DNA. Sequence trace files were aligned and analyzed using Geneious version 7.1.4 created by Biomatters (http://www.geneious.com/).

Cell culture, plasmid transfection and protein analyses

Cells were propagated in DMEM media supplemented with 10% FBS and antibiotics (Life Technologies, Carlsbad, CA). For serum starvation, NIH3T3 cells and human fibroblasts were grown in the presence of 0.1% FBS. Cells were transfected using FuGENE6 according to the manufacturer's protocol (Promega, Madison, WI). pCMV6 vector containing C-terminally FLAG-tagged human ICK was purchased from Origene (Rockville, MD). Site-directed mutagenesis was used to generate the ICK^{E80K} and ICK^{R272Q} mutants according to the manufacturer's protocol (Agilent

Technologies, Santa Clara, CA). To obtain protein samples from mouse tibiae and femurs, the soft tissue was carefully removed, and the proteins were extracted into the lysis buffer (50 mM TrisHCl pH 7.4, 150 mM NaCl, 0.5% NP40, 1 mM EDTA, and 25 mM NaF with proteinase inhibitors and 1mM orthovanadate) on ice for 1 h. The samples were cleared by centrifugation (15,000g/10min), their concentrations were equalized using DC Protein Assay (BioRad, Hercules, CA), and the samples were then mixed 1:1 with 2x Laemmli sample buffer. For Western blotting, cells were lysed in Laemmli sample buffer and protein samples were resolved by SDS-PAGE, transferred onto a PVDF membrane and visualized by chemiluminiscence (Thermo Scientific, Rockford, IL). SAG (smoothened agonist) and PD0325901 were obtained from Tocris Bioscience (Bristol, UK). The following antibodies were used: FLAG (1:1000; Sigma-Aldrich, St. Louis, MO; F1804); $pERK^{T202/Y204}$ (1:1000; Cell Signalling Technology, Beverly, MA; 4370, 4376), ERK (1:1000; Cell Signalling; 9102); actin (1:1000; Cell Signalling; 3700); MEK (1:1000; Santa Cruz Biotechnology, Santa Cruz, CA; sc-219); $pMEK^{S217/S221}$ (1:1000; Cell Signalling; 9121); C-RAF (1:1000; BD Biosciences, San Jose, CA; 610151); $pC\text{-}RAF^{S338}$ (1:1000; Cell Signalling; 9427); GLI3 (1:1000; R&D Systems, Minneapolis, MN; AF3690); $pICK^{Y159}$ (1:1000; Abcam, Cambridge, MA; ab138435).

Immunoprecipitation and kinase assay

HEK293T cells transfected with FLAG-tagged ICK for 11 or 24 h were extracted in buffer containing 50 mM Tris-HCl pH 7.4, 150 mM NaCl, 0.5% NP-40, 0.1% sodium deoxycholate, 2 mM EDTA pH 8.0, 0.5 mM DTT, supplemented with proteinase inhibitors. Extracts were immunoprecipitated with FLAG antibody and immunocomplexes were collected on protein A/G agarose (Santa Cruz) by overnight rotation at 4 °C. Cell-free kinase assays were carried-out with immunoprecipitated ICK or 200 ng of recombinant active ERK2 (Cell Signalling) as a kinase, and 4 μg of recombinant MBP (Sigma) as a substrate, in 25 μl of kinase buffer (50 mM HEPES pH 7.5, 10 mM $MnCl_2$, 10 mM $MgCl_2$, 8 mM β-Glycerophosphate, 1 mM DTT, 0.1 mM Na_3VO_4, 0.1 mM PMSF) for 30 min at 37 °C in the presence of 1 μCi ^{32}P-ATP (Izotop, Budapest, Hungary). Samples were resolved by SDS-PAGE and visualized by autoradiography.

Immunocytochemistry

Cells were plated on glass coverslips in 24 well plates, transfected with 0.25-2 μg of ICK plasmid for 20 h, fixed with 4% paraformaldehyde, blocked with 10% goat serum (Life Technologies) and incubated with the following primary antibodies at 4 °C overnight: FLAG (1:200; Sigma-Aldrich F1804), detyrosinated tubulin (1:1000; Millipore, Billerica, MA; AB3201), acetylated α-tubulin (1:500; Life Technologies 32-2700), polyglutamylated tubulin (1:300; Adipogen, San Diego, CA; GT335), ARL13B (1:250; Proteintech, Rosemont, IL; 17711-1-AP), pericentrin (1:2500; Abcam ab4448), and GLI3 (1:50; R&D Systems AF3690). Secondary antibodies were Alexa Fluor 488/594-conjugated secondary antibodies (1:500; Life Technologies). Images were taken on an LSM700 laser scanning microscope with acquisition done using ZEN Black 2012 software. Image data were acquired as Z-stacks of images with 0.3 μm distance between neighbouring z-sections. Measurements of cilia length in 3D were conducted in ImageJ (NIH) using plugin View5D by Rainer Heintzmann (King's College London, UK). For calculation of the GLI3 signal at the cilia tip, Z-stacks of cilia images were acquired using 63x oil immersion objective. 3D volume analysis was not performed due to the small GLI3 signal area allowing only 1 to 3 Z-sections to be taken. Instead, the Z-section best representing the GLI3 signal distribution was used to measure the area size using automatic thresholding by the intermodes method in ImageJ.

Histology and immunohistochemistry

For histology, femurs from newborn mice were fixed by cryosubstitution in methanol for immunohistochemistry (70) and PFA (4%) for histochemistry. Samples were decalcified in 10% formic acid. For immunohistochemistry, paraffin sections were treated with citrate buffer for antigen retrieval and quenched by peroxidase solution. The Histostain Plus kit with DAB as a chromogen (Invitrogen) was used for ICK antibody (1:150; Sigma; HPA001113) staining. $Ick^{tm1a(KOMP)Mbp}$ mice were crossed with Rosa26-FLP1 mice which express FLP1 recombinase under the control of Rosa26. Then the exon 6 deleted ICK null allele, $Ick^{-/-}$, was generated by crossing this conditional allele with EIIA-driven Cre recombinase transgenic mice. $Ick^{-/-}$ and control mouse sections were stained with picrosirius red for 1 h and hematoxylin for contrast.

Scanning electron microscopy

Cells were fixed in 3% glutaraldehyde (Polysciences, Warrington, USA) dissolved in 0.2 M cacodylate buffer (Spi supplies/Structure Probe, West Chester, USA) for 2 h at room temperature and postfixed in 1% (v/v) osmium tetraoxide (Degussa, Hanau, Germany) for 30 min at 22 °C. The samples were washed in 0.2 M cacodylate buffer, dehydrated in ascending ethanol grade and dried in a Critical Point Dryer (Balzers Union Limited, Balzers, Liechtenstein) using liquid carbon dioxide. Samples were sputtered with gold in Sputter Coater (Balzers) and subsequently examined using scanning electron microscopy (Tescan Orsay Holding, Brno, Czech Republic).

Structural modelling

The three-dimensional models for wild-type and ICK^{E80K} were generated by template-based (PDB ID: 3PFQ) homology modelling using the PHYRE software (71). The ICK-specific functional elements, predicted using the NCBI Conserved Domain Database (72), were mapped onto a three-dimensional model of ICK using the CHIMERA software (73). Template based (PDB ID: 3C4W, 1JNK) homology modelling was employed to dock ATP into the ATP-binding site of ICK.

In situ hybridization and quantitative RT-PCR

Limbs from control or $Ick^{-/-}$ embryo (E18.5) were fixed with 4% PFA in PBS for 3 days, decalcified with 0.5M EDTA in RNAse-free water, and embedded for cryosection. Sections were then hybridized with digoxigenin-labelled antisense RNA probes followed by incubation in anti-Dig antibody conjugated with alkaline phosphatase. Colorimetric reaction was carried out using NBT/BCIP as the substrate. Riboprobes for *Gli1*, *Ihh* and *Ptch1* were prepared as previously described (74, 75). Total RNA was isolated using RNeasy Mini Kit (Qiagen, Hilden, DE) and transcribed into cDNA using Transcriptor First Strand cDNA Synthesis Kit (Roche, Basel, CH). For quantitative PCR, LightCycler® 480 SYBER Green I Master (Roche) was used together with the following QuantiTect Primer Assays (Qiagen):

Hs_PTCH1_1_SG (QT00075824), Hs_GLI1_1_SG (QT00060501), and Hs_GAPDH_vb.1_SG (QT02504278). ΔΔCT method was used for data quantification.

Supplementary Material

Supplementary Material is available at *HMG* online.

Acknowledgements

We thank Dobromila Klemova and Ladislav Ilkovics for help with electron microscopy, Miriam Minarikova for technical assistance and Jakub Pivnicka for help with data analysis.

Conflict of Interest statement. None declared.

Funding

This work was supported in part by NIH grants RO1 AR066124, R01AR062651, and RO1 DE019567 to D.H.C. and D.K. Sequencing was provided by the University of Washington Center for Mendelian Genomics (UW-CMG) and was funded by the National Human Genome Research Institute and the National Heart, Lung and Blood Institute grant 2UM1HG006493 to Drs. Debbie Nickerson, Michael Bamshad, and Suzanne Leal.
The NIH Training Grant in Genomic Analysis and Interpretation T32 HG002536 supported S.P.T. The work was also supported by the Ministry of Education, Youth and Sports of the Czech Republic (KONTAKT LH12004, LH15231), the Grant Agency of Masaryk University (0071-2013), the European Regional Development Fund (FNUSA-ICR No.CZ.1.05/1.1.00/02.0123; CEITEC No. CZ.1.05/1.100/02.0068) and European Union (ICRC-ERA-HumanBridge No.316345). A Career Development Grant from the European Organization for Molecular Biology (IG2535) and the Netherlands Organization for Scientific Research (VIDI) supported L.T. L.T. was supported by CEITEC 2020 (LQ1601) project with financial contributions made by the Ministry of Education, Youths and Sports of the Czech Republic within special support paid from the National Programme for Sustainability II funds. Junior researcher funds from the Faculty of Medicine MU supported M.K.B. This research was also supported in part by NIH/National Center for Advancing Translational Science (NCATS) UCLA CTSI Grant Number UL1TR000124 and by Korea Mouse Phenotyping Project (NRF-2014M3A9D5A01073969) of the Ministry of Science, ICT and Future Planning through the National Research Foundation.

References

1. Provot, S. and Schipani, E. (2005) Molecular mechanisms of endochondral bone development. *Biochem. Biophys. Res. Commun.*, **328**, 658–865.
2. Bonafe, L., Cormier-Daire, V., Hall, C., Lachman, R., Mortier, G., Mundlos, S., Nishimura, G., Sangiorgi, L., Savarirayan, R., Sillence, D., *et al.* (September 23, 2015) Nosology and classification of genetic skeletal disorders: 2015 revision. *Am. J. Med. Genet. A*, 10.1002/ajmg.a.37365.
3. Huber, C. and Cormier-Daire, V. (2012) Ciliary disorder of the skeleton. *Am. J. Med. Genet. C Semin. Med. Genet.*, **160C**, 165–174.
4. Beales, P.L., Bland, E., Tobin, J.L., Bacchelli, C., Tuysuz, B., Hill, J., Rix, S., Pearson, C.G., Kai, M Hartley, J., *et al.* (2007) IFT80, which encodes a conserved intraflagellar transport protein, is mutated in Jeune asphyxiating thoracic dystrophy. *Nat. Genet.*, **39**, 727–729.
5. Cavalcanti, D.P., Huber, C., Sang, K.H., Baujat, G., Collins, F., Delezoide, A.L., Dagoneau, N. L., Merrer, M., Martinovic, J. Mello, M.F., *et al.* (2011) Mutation in IFT80 in a fetus with the phenotype of Verma-Naumoff provides molecular evidence for Jeune-Verma-Naumoff dysplasia spectrum. *J. Med. Genet.*, **48**, 88–92.
6. Bredrup, C., Saunier, S., Oud, M.M., Fiskerstrand, T., Hoischen, A., Brackman, D., Leh, S.M., Midtbø, M., Filhol, E., Bole-Feysot, C., *et al.* (2011) Ciliopathies with skeletal anomalies and renal insufficiency due to mutations in the IFT-A gene WDR19. *Am. J. Hum. Genet.*, **89**, 634–643.
7. Huber, C., Wu, S., Kim, A.S., Sigaudy, S., Sarukhanov, A., Serre, V., Baujat, G.L., Quan Sang, K.H. Rimoin, D.L., Cohn D.H., *et al.* (2013) WDR34 mutations that cause short-rib polydactyly syndrome type III/severe asphyxiating thoracic dysplasia reveal a role for the NF-κB pathway in cilia. *Am. J. Hum. Genet.*, **93**, 926–931.
8. Schmidts, M., Vodopiutz, J., Christou-Savina, S., Cortés, C.R., McInerney-Leo, A.M., Emes, R.D., Arts, H.H., Tüysüz, B., D'Silva, J., Leo, P.J., *et al.* (2013) Mutations in the gene encoding IFT dynein complex component WDR34 cause Jeune asphyxiating thoracic dystrophy. *Am. J. Hum. Genet.*, **93**, 932–944.
9. Gilissen, C., Arts, H.H., Hoischen, A., Spruijt, L., Mans, D.A., Arts, P., van Lier, B., Steehouwer, M., van Reeuwijk, J., Kant, S.G., *et al.* (2010) Exome sequencing identifies WDR35 variants involved in Sensenbrenner syndrome. *Am. J. Hum. Genet.*, **87**, 418–423.
10. Mill, P., Lockhart, P.J., Fitzpatrick, E., Mountford, H.S., Hall, E.A., Reijns, M.A., Keighren, M., Bahlo, M., Bromhead, C.J., Budd, P., *et al.* (2011) Human and mouse mutations in WDR35 cause short-rib polydactyly syndromes due to abnormal ciliogenesis. *Am. J. Hum. Genet.*, **88**, 508–515.
11. Perrault, I., Saunier, S., Hanein, S., Filhol, E., Bizet, A.A., Collins, F., Salih, M.A., Gerber, S., Delphin, N., Bigot, K., *et al.* (2012) Mainzer-Saldino syndrome is a ciliopathy caused by IFT140 mutations. *Am. J. Hum. Genet.*, **90**, 864–870.
12. Schmidts, M., Frank, V., Eisenberger, T., Al Turki, S., Bizet, A.A., Antony, D., Rix, S., Decker, C., Bachmann, N., Bald, M., *et al.* (2013) Combined NGS approaches identify mutations in the intraflagellar transport gene IFT140 in skeletal ciliopathies with early progressive kidney Disease. *Hum. Mutat.*, **34**, 714–724.
13. Halbritter, J., Bizet, A.A., Schmidts, M., Porath, J.D., Braun, D.A., Gee, H.Y., McInerney-Leo, A.M., Krug, P., Filhol, E., Davis, E.E., *et al.* (2013) Defects in the IFT-B component IFT172 cause Jeune and Mainzer-Saldino syndromes in humans. *Am. J. Hum. Genet.*, **93**, 915–925.
14. McInerney-Leo, A.M., Schmidts, M., Cortés, C.R., Leo, P.J., Gener, B., Courtney, A.D., Gardiner, B., Harris, J.A., Lu, Y., Marshall, M., *et al.* (2013) Short-rib polydactyly and Jeune syndromes are caused by mutations in WDR60. *Am. J. Hum. Genet.*, **93**, 515–523.
15. Davis, E.E., Zhang, Q., Liu, Q., Diplas, B.H., Davey, L.M., Hartley, J., Stoetzel, C., Szymanska, K., Ramaswami, G., Logan, C.V., *et al.* (2011) TTC21B contributes both causal and modifying alleles across the ciliopathy spectrum. *Nat. Genet.*, **43**, 189–196.
16. Dagoneau,N., Goulet,M., Geneviève,D., Sznajer,Y., Martinovic,J., Smithson,S., Huber,C., Baujat,G., Flori,E., Tecco,L. *et al.* (2009) DYNC2H1 mutations cause asphyxiating thoracic dystrophy and short rib-polydactyly syndrome, type III. *Am. J. Hum. Genet.*, **84**, 706–711.
17. Merrill, A.E., Merriman, B., Farrington-Rock, C., Camacho, N., Sebald, E.T., Funari, V.A., Schibler, M.J., Firestein, M.H., Cohn,

Z.A., Priore, M.A., *et al*. (2009) Ciliary abnormalities due to defects in the retrograde transport protein DYNC2H1 in short-rib polydactyly syndrome. *Am. J. Hum. Genet.*, **84**, 542–549.
18. Taylor, S.P., Dantas, T.J., Duran, I., Wu, S. and Lachman, R.S., University of Washington Center for Mendelian Genomics Consortium, Nelson,S.F., Cohn,D.H., Vallee,R.B., and Krakow,D. (2015) Mutations in DYNC2LI1 disrupt cilia function and cause short rib polydactyly syndrome. *Nat. Commun.*, **6**, 7092.
19. Shaheen, R., Schmidts, M., Faqeih, E., Hashem, A., Lausch, E., Holder, I., Superti-Furga, A.U.K.10K., Consortium, Mitchison, H.M., Almoisheer, A., *et al*. (2015) A founder CEP120 mutation in Jeune asphyxiating thoracic dystrophy expands the role of centriolar proteins in skeletal ciliopathies. *Hum. Mol. Genet.*, **24**, 1410–1419.
20. Malicdan, M.C., Vilboux, T., Stephen, J., Maglic, D., Mian, L., Konzman, D., Guo, J., Yildirimli, D., Bryant, J., Fischer, R., *et al*. (September 18, 2015) Mutations in human homologue of chicken talpid3 gene (KIAA0586) cause a hybrid ciliopathy with overlapping features of Jeune and Joubert syndromes. *J. Med. Genet.*, 10.1136/jmedgenet-2015-103316.
21. Alby, C., Piquand, K., Huber, C., Megarbané, A., Ichkou, A., Legendre, M., Pelluard, F., Encha-Ravazi, F., Abi-Tayeh, G., Bessières, B., *et al*. (2015) Mutations in KIAA0586 Cause Lethal Ciliopathies Ranging from a Hydrolethalus Phenotype to Short-Rib Polydactyly Syndrome. *Am. J. Hum. Genet.*, **97**, 311–318.
22. Fu, Z., Kim, J., Vidrich, A., Sturgill, T.W. and Cohn, S.M. (2009) Intestinal cell kinase, a MAP kinase-related kinase, regulates proliferation and G1 cell cycle progression of intestinal epithelial cells. *Am. J. Physiol. Gastrointest. Liver Physiol.*, **297**, G632–G640.
23. Yang, Y., Roine, N. and Mäkelä, T.P. (2013) CCRK depletion inhibits glioblastoma cell proliferation in a cilium-dependent manner. *EMBO Rep.*, **14**, 741–747.
24. Burghoorn, J., Dekkers, M.P., Rademakers, S., de Jong, T., Willemsen, R. and Jansen, G. (2007) Mutation of the MAP kinase DYF-5 affects docking and undocking of kinesin-2 motors and reduces their speed in the cilia of Caenorhabditis elegans. *Proc. Natl. Acad. Sci. U. S. A*, **104**, 7157–7162.
25. Berman, S.A., Wilson, N.F., Haas, N.A. and Lefebvre, P.A. (2003) A novel MAP kinase regulates flagellar length in Chlamydomonas. *Curr. Biol.*, **13**, 1145–1149.
26. Bengs, F., Scholz, A., Kuhn, D. and Wiese, M. (2005) LmxMPK9, a mitogen-activated protein kinase homologue affects flagellar length in Leishmania mexicana. *Mol. Microbiol.*, **55**, 1606–1615.
27. Lahiry, P., Wang, J., Robinson, J.F., Turowec, J.P., Litchfield, D.W., Lanktree, M.B., Gloor, G.B., Puffenberger, E.G., Strauss, K.A., Martens, M.B., *et al*. (2009) A multiplex human syndrome implicates a key role for intestinal cell kinase in development of central nervous, skeletal, and endocrine systems. *Am. J. Hum. Genet.*, **84**, 134–147.
28. Oud, M.M., Bonnard, C., Mans, D.A., Altunoglu, U., Tohari, S., Ng, A.Y., Eskin, A., Lee, H., Rupar, C.A., de Wagenaar, N.P., *et al*. (2016) A novel ICK mutation causes ciliary disruption and lethal endocrine-cerebro-osteodysplasia syndrome. *Cilia*, **5**, doi: 10.1186/s13630-016-0029-1.
29. Moon, H., Song, J., Shin, J.O., Lee, H., Kim, H.K., Eggenschwiller, J.T., Bok, J. and Ko, H.W. (2014) Intestinal cell kinase, a protein associated with endocrine-cerebro-osteodysplasia syndrome, is a key regulator of cilia length and Hedgehog signaling. *Proc. Natl. Acad. Sci. U. S. A.*, **111**, 8541–8546.
30. Chaya, T., Omori, Y., Kuwahara, R. and Furukawa, T. (2014) ICK is essential for cell type-specific ciliogenesis and the regulation of ciliary transport. *Embo J.*, **33**, 1227–1242.
31. Fu, Z., Larson, K.A., Chitta, R.K., Parker, S.A., Turk, B.E., Lawrence, M.W., Kaldis, P., Galaktionov, K., Cohn, S.M., Shabanowitz, J., *et al*. (2006) Identification of yin-yang regulators and a phosphorylation consensus for male germ cell-associated kinase (MAK)-related kinase. *Mol. Cell. Biol.*, **26**, 8639–8654.
32. Fu, Z., Schroeder, M.J., Shabanowitz, J., Kaldis, P., Togawa, K., Rustgi, A.K., Hunt, D.F. and Sturgill, T.W. (2005) Activation of a nuclear Cdc2-related kinase within a mitogen-activated protein kinase-like TDY motif by autophosphorylation and cyclin-dependent protein kinase-activating kinase. *Mol. Cell. Biol.*, **25**, 6047–6064.
33. Wang, L.Y. and Kung, H.J. (2012) Male germ cell-associated kinase is overexpressed in prostate cancer cells and causes mitotic defects via deregulation of APC/C-CDH1. *Oncogene*, **31**, 2907–2918.
34. Broekhuis, J.R., Verhey, K.J. and Jansen, G. (2014) Regulation of cilium length and intraflagellar transport by the RCK-kinases ICK and MOK in renal epithelial cells. *PLoS One.*, **9**, e108470.
35. Chen, J.K., Taipale, J., Young, K.E., Maiti, T. and Beachy, P.A. (2002) Small molecule modulation of Smoothened activity. *Proc. Natl. Acad. Sci. U. S. A.*, **99**, 14071–14076.
36. Kronenberg, H.M. (2006) PTHrP and skeletal development. *Ann. N. Y. Acad. Sci.*, **1068**, 1–13.
37. Krejci, P., Salazar, L., Goodridge, H.S., Kashiwada, T.A., Schibler, M.J., Jelinkova, P., Thompson, L.M. and Wilcox, W.R. (2008) STAT1 and STAT3 do not participate in FGF-mediated growth arrest in chondrocytes. *J. Cell Sci.*, **121**, 272–281.
38. Krejci, P., Prochazkova, J., Smutny, J., Chlebova, K., Lin, P., Aklian, A., Bryja, V., Kozubik, A. and Wilcox, W.R. (2010) FGFR3 signaling induces a reversible senescence phenotype in chondrocytes similar to oncogene-induced premature senescence. *Bone*, **47**, 102–110.
39. He, M., Subramanian, R., Bangs, F., Omelchenko, T., Liem, K.F., Jr., Kapoor, T.M. and Anderson, K.V. (2014) The kinesin-4 protein Kif7 regulates mammalian Hedgehog signalling by organizing the cilium tip compartment. *Nat. Cell Biol.*, **16**, 663–672.
40. Rosenbaum, J.L. and Witman, G.B. (2002) Intraflagellar transport. *Nat. Rev. Mol. Cell Biol.*, **3**, 813–825.
41. Pazour, G.J. and Bloodgood, R.A. (2008) Targeting proteins to ciliary membrane. *Curr. Top. Dev. Biol.*, **85**, 115–149.
42. Dishinger, J.F., Kee, H.L., Jenkins, P.M., Fan, S., Hurd, T.W., Hammond, J.W., Truong, Y.N., Margolis, B., Martens, J.R. and Verhey, K.J. (2010) Ciliary entry of the kinesin-2 motor KIF17 is regulated by importin-beta2 and RanGTP. *Nat. Cell. Biol.*, **12**, 703–710.
43. Wong, S.Y. and Reiter, J.F. (2008) The primary cilium at the crossroads of mammalian hedgehog signaling. *Curr. Top. Dev. Biol.*, **85**, 225–260.
44. te Welscher, P., Zuniga, A., Kuijper, S., Drenth, T., Goedemans, H.J., Meijlink, F. and Zeller, R. (2002) Progression of vertebrate limb development through SHH-mediated counteraction of GLI3. *Science*, **298**, 827–830.
45. Haycraft, C.J., Zhang, Q., Song, B., Jackson, W.S., Detloff, P.J., Serra, R. and Yoder, B.K. (2007) Intraflagellar transport is essential for endochondral bone formation. *Development*, **134**, 307–316.
46. Liu, A., Wang, B. and Niswander, L.A. (2005) Mouse intraflagellar transport proteins regulate both the activator and repressor functions of Gli transcription factors. *Development*, **132**, 3103–3111.
47. Jia, J., Kolterud, A., Zeng, H., Hoover, A., Teglund, S., Toftgård, R. and Liu, A. (2009) Suppressor of Fused inhibits

mammalian Hedgehog signaling in the absence of cilia. *Dev. Biol.*, **330**, 452–460.
48. Hoover, A.N., Wynkoop, A., Zeng, H., Jia, J., Niswander, L.A. and Liu, A. (2008) C2cd3 is required for cilia formation and Hedgehog signaling in mouse. *Development*, **135**, 4049–4058.
49. Huangfu, D. and Anderson, K.V. (2005) Cilia and Hedgehog responsiveness in the mouse. *Proc. Natl. Acad. Sci. U. S. A.*, **102**, 11325–11330.
50. Heydeck, W., Zeng, H. and Liu, A. (2009) Planar cell polarity effector gene Fuzzy regulates cilia formation and Hedgehog signal transduction in mouse. *Dev. Dyn.*, **238**, 3035–3042.
51. Cortellino, S., Wang, C., Wang, B., Bassi, M.R., Caretti, E., Champeval, D., Calmont, A., Jarnik, M., Burch, J., Zaret, K.S., *et al.* (2009) Defective ciliogenesis, embryonic lethality and severe impairment of the Sonic Hedgehog pathway caused by inactivation of the mouse complex A intraflagellar transport gene Ift122/Wdr10, partially overlapping with the DNA repair gene Med1/Mbd4. *Dev. Biol.*, **325**, 225–237.
52. Cheung, H.O., Zhang, X., Ribeiro, A., Mo, R., Makino, S., Puviindran, V., Law, K.K., Briscoe, J. and Hui, C.C. (2009) The kinesin protein Kif7 is a critical regulator of Gli transcription factors in mammalian hedgehog signaling. *Sci. Signal.*, **2**, ra29.
53. Endoh-Yamagami, S., Evangelista, M., Wilson, D., Wen, X., Theunissen, J.W., Phamluong, K., Davis, M., Scales, S.J., Solloway, M.J., de Sauvage, F.J., *et al.* (2009) The mammalian Cos2 homolog Kif7 plays an essential role in modulating Hh signal transduction during development. *Curr. Biol.*, **19**, 1320–1326.
54. Liem, K.F., Jr., He, M., Ocbina, P.J. and Anderson, K.V. (2009) Mouse Kif7/Costal2 is a cilia-associated protein that regulates Sonic hedgehog signaling. *Proc. Natl. Acad. Sci. U. S. A.*, **106**, 13377–13382.
55. Tukachinsky, H., Lopez, L.V. and Salic, A. (2010) A mechanism for vertebrate Hedgehog signaling: recruitment to cilia and dissociation of SuFu-Gli protein complexes. *J. Cell Biol.*, **191**, 415–428.
56. Wilcox, W.R., Tavormina, P.L., Krakow, D., Kitoh, H., Lachman, R.S., Wasmuth, J.J., Thompson, L.M. and Rimoin, D.L. (1998) Molecular, radiologic, and histopathologic correlations in thanatophoric dysplasia. *Am. J. Med. Genet.*, **78**, 274–281.
57. Krejci, P. (2014) The paradox of FGFR3 signaling in skeletal dysplasia: why chondrocytes growth arrest while other cells over proliferate. *Mutat. Res. Rev. Mutat. Res.*, **759**, 40–48.
58. Chen, Z., Yue, S.X., Zhou, G., Greenfield, E.M. and Murakami, S. (2015) ERK1 and ERK2 regulate chondrocyte terminal differentiation during endochondral bone formation. *J. Bone Miner. Res.*, **30**, 765–774.
59. Thiel, C., Kessler, K., Giessl, A., Dimmler, A., Shalev, S.A., von der Haar, S., Zenker, M., Zahnleiter, D., Stöss, H., Beinder, E., *et al.* (2011) NEK1 mutations cause short-rib polydactyly syndrome type majewski. *Am. J. Hum. Genet.*, **88**, 106–114.
60. White, M.C. and Quarmby, L.M. (2008) The NIMA-family kinase, Nek1 affects the stability of centrosomes and ciliogenesis. *BMC Cell Biol.*, **9**, 29.
61. Letwin, K., Mizzen, L., Motro, B., Ben-David, Y., Bernstein, A. and Pawson, T. (1992) A mammalian dual specificity protein kinase, Nek1, is related to the NIMA cell cycle regulator and highly expressed in meiotic germ cells. *Embo J.*, **11**, 3521–3531.
62. McKenna, A., Hanna, M., Banks, E., Sivachenko, A., Cibulskis, K., Kernytsky, A., Garimella, K., Altshuler, D., Gabriel, S., Daly, M., *et al.* (2010) The Genome Analysis Toolkit: a MapReduce framework for analyzing next-generation DNA sequencing data. *Genome. Res.*, **20**, 1297–1303.
63. DePristo, M.A., Banks, E., Poplin, R., Garimella, K.V., Maguire, J.R., Hartl, C., Philippakis, A.A., del Angel, G., Rivas, M.A., Hanna, M., *et al.* (2011) A framework for variation discovery and genotyping using next-generation DNA sequencing data. *Nat. Genet.*, **43**, 491–498.
64. Van der Auwera, G.A., Carneiro, M.O., Hartl, C., Poplin, R., Del Angel, G., Levy-Moonshine, A., Jordan, T., Shakir, K., Roazen, D., Thibault, J., *et al.* (2013) From FastQ data to high confidence variant calls: the Genome Analysis Toolkit best practices pipeline. *Curr. Protoc. Bioinformatics*, **11**, 11.10.1–11.10.33.
65. Yourshaw, M., Taylor, S.P., Rao, A.R., Martín, M.G. and Nelson, S.F. (2015) Rich annotation of DNA sequencing variants by leveraging the Ensembl Variant Effect Predictor with plugins. *Brief Bioinform.*, **16**, 255–264.
66. Adzhubei, I.A., Schmidt, S., Peshkin, L., Ramensky, V.E., Gerasimova, A., Bork, P., Kondrashov, A.S. and Sunyaev, S.R. (2010) A method and server for predicting damaging missense mutations. *Nat. Methods*, **7**, 248–249.
67. Kumar, P., Henikoff, S. and Ng, P.C. (2009) Predicting the effects of coding non-synonymous variants on protein function using the SIFT algorithm. *Nat. Protoc.*, **4**, 1073–1081.
68. González-Pérez, A. and López-Bigas, N. (2011) Improving the assessment of the outcome of nonsynonymous SNVs with a consensus deleteriousness score, Condel. *Am. J. Hum. Genet.*, **88**, 440–449.
69. Kircher, M., Witten, D.M., Jain, P., O'Roak, B.J., Cooper, G.M. and Shendure, J. (2014) A general framework for estimating the relative pathogenicity of human genetic variants. *Nat. Genet.*, **46**, 310–315.
70. Duran, I., Marí-Beffa, M., Santamaría, J.A., Becerra, J. and Santos-Ruiz, L. (2011) Freeze substitution followed by low melting point wax embedding preserves histomorphology and allows protein and mRNA localization techniques. *Microsc. Res. Tech.*, **74**, 440–448.
71. Kelley, L.A. and Sternberg, M.J. (2009) Protein structure prediction on the Web: a case study using the Phyre server. *Nat. Protoc.*, **4**, 363–371.
72. Marchler-Bauer, A., Zheng, C., Chitsaz, F., Derbyshire, M.K., Geer, L.Y., Geer, R.C., Gonzales, N.R., Gwadz, M., Hurwitz, D.I., Lanczycki, C.J., *et al.* (2013) CDD: conserved domains and protein three-dimensional structure. *Nucleic Acids Res.*, **41**, D348–D352.
73. Pettersen, E.F., Goddard, T.D., Huang, C.C., Couch, G.S., Greenblatt, D.M., Meng, E.C. and Ferrin, T.E. (2004) UCSF Chimera - a visualization system for exploratory research and analysis. *J. Comput. Chem.*, **25**, 1605–1612.
74. Hui, C.C. and Joyner, A.L. (1993) A mouse model of greig cephalopolysyndactyly syndrome: the extra-toesJ mutation contains an intragenic deletion of the Gli3 gene. *Nat. Genet.*, **3**, 241–246.
75. Milenkovic, L., Goodrich, L.V., Higgins, K.M. and Scott, M.P. (1999) Mouse patched1 controls body size determination and limb patterning. *Development*, **126**, 4431–4440.